

## Article

# Comparative Study of High-Cycle Fatigue and Failure Mechanisms in Ultrahigh-Strength CrNiMoWMnV Low-Alloy Steels

Atef Hamada <sup>1,\*</sup>, Mohammed Ali <sup>2,3</sup>, Sumit Ghosh <sup>2</sup>, Matias Jaskari <sup>1</sup>, Tarek Allam <sup>4</sup>, Ruth Schwaiger <sup>4</sup>, Mamdouh Eissa <sup>3</sup> and Taha Mattar <sup>3</sup>

<sup>1</sup> Future Manufacturing Technologies, Kerttu Saalasti Institute, University of Oulu, FI-85500 Nivala, Finland; matias.jaskari@oulu.fi

<sup>2</sup> Materials and Mechanical Engineering Centre for Advanced Steels Research, University of Oulu, FI-90014 Oulu, Finland; mohammed.ali@oulu.fi (M.A.); sumit.ghosh@oulu.fi (S.G.)

<sup>3</sup> Steel Technology Department, Central Metallurgical Research and Development Institute, Helwan 11421, Egypt; mamdouh.eissa@gmail.com (M.E.); taha.mattar@gu.edu.eg (T.M.)

<sup>4</sup> Microstructure and Properties of Materials (IMD-1), Institute of Energy Materials and Devices (IMD), Forschungszentrum Jülich GmbH, 52425 Jülich, Germany; t.allam@fz-juelich.de (T.A.); r.schwaiger@fz-juelich.de (R.S.)

\* Correspondence: atef.hamadasaleh@oulu.fi; Tel.: +358-45251-6553

**Abstract:** This study provides a thorough analysis of the fatigue resistance of two low-alloy ultrahigh-strength steels (UHSSs): Steel A (fully martensitic) and Steel B (martensitic–bainitic). The investigation focused on the fatigue behaviour, damage mechanisms, and failure modes across different microstructures. Fatigue strength was determined through fully reversed tension–compression stress-controlled fatigue tests. Microstructural evolution, fracture surface characteristics, and crack-initiation mechanisms were investigated using laser scanning confocal microscopy and scanning electron microscopy. Microindentation hardness ( $H_{IT}$ ) tests were conducted to examine the cyclic hardening and softening of the steels. The experimental results revealed that Steel A exhibited superior fatigue resistance compared to Steel B, with fatigue limits of 550 and 500 MPa, respectively. Fracture surface analysis identified non-metallic inclusions (NMIs) comprising the complex MnO–SiO<sub>2</sub> as critical sites for crack initiation during cyclic loading in both steels. The  $H_{IT}$  results after fatigue indicated significant cyclic softening for Steel A, with  $H_{IT}$  values decreasing from  $7.7 \pm 0.36$  to  $5.66 \pm 0.26$  GPa. In contrast, Steel B exhibited slight cyclic hardening, with  $H_{IT}$  values increasing from  $5.24 \pm 0.23$  to  $5.41 \pm 0.31$  GPa. Furthermore, the martensitic steel demonstrated superior yield and tensile strengths of 1145 and 1870 MPa, respectively. Analysis of the fatigue behaviour revealed the superior fatigue resistance of martensitic steel. The complex morphology and shape of the NMIs, examined using the 3D microstructure characterisation technique, demonstrated their role as stress concentrators, leading to localised plastic deformation and crack initiation.

**Keywords:** ultrahigh-strength steel; fatigue resistance; martensite–bainite; non-metallic inclusions; microstructure



**Citation:** Hamada, A.; Ali, M.; Ghosh, S.; Jaskari, M.; Allam, T.; Schwaiger, R.; Eissa, M.; Mattar, T. Comparative Study of High-Cycle Fatigue and Failure Mechanisms in Ultrahigh-Strength CrNiMoWMnV Low-Alloy Steels. *Metals* **2024**, *14*, 1238. <https://doi.org/10.3390/met14111238>

Academic Editors: Antonio Mateo and Giovanni Meneghetti

Received: 7 September 2024

Revised: 24 October 2024

Accepted: 28 October 2024

Published: 29 October 2024



**Copyright:** © 2024 by the authors. Licensee MDPI, Basel, Switzerland. This article is an open access article distributed under the terms and conditions of the Creative Commons Attribution (CC BY) license (<https://creativecommons.org/licenses/by/4.0/>).

## 1. Introduction

Ultrahigh-strength steels (UHSSs) with low-alloying elements have emerged as key materials in the field of structural engineering, offering exceptional strength properties with a minimum yield strength of 1 GPa. These steels have several advantages over high-alloy steels, including improved availability and lower costs [1]. The combination of high strength, acceptable toughness, good formability, and weldability makes UHSS an attractive option for a wide range of structural applications, including pressure vessels, pipelines, shipbuilding, offshore structures, automotive components, nuclear power reactors, bridges, and lifting/handling equipment [2,3]. Moreover, UHSS's high strength-to-weight ratio

positions it as a promising candidate for sustainable materials in various industries, such as mining machinery, construction machinery, automobiles, and armoured vehicles [4].

To achieve the desired mechanical properties, UHSSs are designed with a specific range of chemical compositions and processing routes. The quenching process was employed to promote a hard lath martensitic structure, which was accomplished by controlling the carbon content within the range of 0.2–0.3 wt.% and incorporating microalloying elements like Cr, Mo, and W. The presence of nanosized carbides further enhances the performance of the material [5].

Among the critical mechanical properties that determine the suitability of structural materials in service, fatigue strength plays a crucial role. Fatigue damage is the primary cause of structural material failure [6,7]. Therefore, understanding the fatigue behaviour and damage mechanisms of UHSS has become a subject of significant interest for researchers aiming to improve the resistance of the material to failure under cyclic loading conditions.

Several studies have investigated the fatigue behaviour of UHSSs and the role of non-metallic inclusions (NMIs) in fatigue crack initiation and propagation. For instance, Yu et al. [8] conducted a comprehensive analysis of the fatigue behaviour of UHSS with a superior strength of 2 GPa in very-high-cycle regimes. Their findings highlighted the beneficial effects of cleanliness from oxides and tempering at higher temperatures in enhancing fatigue resistance. Okuda et al. [9] focused on the bending fatigue behaviour of the UHSS types commonly employed in the automotive industry, including bainitic steel, martensitic steel, and precipitation-hardened steel. The study revealed that precipitation-hardening steel exhibited a fatigue strength 100–150 MPa higher than that of other steels, underscoring the impact of the phase structure on the fatigue performance. Schönbauer et al. [10] investigated the fatigue behaviour of UHSS, specifically Type Ck45M, under uniaxial and torsional loading in a high-cycle regime. Their study demonstrated a fatigue limit of 600 MPa under a load ratio of  $R = -1$ . Shiozawa et al. [11] focused on subsurface crack initiation and propagation in UHSS, where multiple fatigue microcracks were initiated around the NMIs, leading to coalescence. Hong et al. [12] examined fatigue crack initiation in high-strength steels under rotating–bending and ultrasonic axial cycling, highlighting the significant influence of the inclusion size on the fatigue life and crack extension rate. In a subsequent investigation conducted by Hong et al. [13], the microscopic characteristics of the crack initiation region surrounding the NMI in two UHSSs were examined. This study reveals the presence of a nanograin layer with a thickness ranging from 500 to 800 nm. The size of the nanograins is approximately 50 nm. Remarkably, the nanograin layer was observed on both sides of the fractured surface in the fine granular area (FGA) region. Furuya et al. [14] explored the gigacycle fatigue properties of UHSS at various frequencies and found that the fatigue properties were independent of the frequency, with all specimens failing owing to internal inclusions. A review report by Jeddi and Palin-Luc [15] emphasised the critical role of internal inclusions in the very-high-cycle fatigue (VHCF) of high-strength steels, acting as “notches” compared to the role of cyclic plastic deformation at the surface. Gui et al. [16] studied high-cycle and very-high-cycle fatigue in UHSS with a bainite/martensite multiphase structure, emphasising the predominant role of inclusions in fatigue crack initiation, particularly in specimens with large inclusion sizes. Liu et al. [17] investigated the fatigue behaviour of a novel ultrahigh-strength steel and identified two failure mechanisms: surface-defect-induced failure caused by machining marks and interior matrix failure associated with defects larger than 3.3  $\mu\text{m}$ .

Collectively, these studies underscore the significance of NMIs in the fatigue mechanisms of high-strength steels, with implications for fatigue life and crack initiation. Understanding these mechanisms is crucial for improving the fatigue performance of these steels and ensuring their reliable application in various engineering structures.

Furthermore, researchers have investigated the impact of hierarchical martensitic microstructures on fatigue strength and crack growth in UHSSs. For instance, Yuan et al. [18] conducted a comprehensive study on type 22MnB5 hot stamping steels with a remarkable yield strength and ultimate tensile strength of approximately 1.1 and 1.4 GPa, respectively.

They attributed the effective control of fatigue crack growth behaviour to the presence of block components within the martensitic structure. Similarly, Hojo et al. [19] explored the effects of the phase matrix structure and nitrogen addition on the fatigue properties of UHSS. Their investigation revealed that martensitic and bainitic–martensite steel structures exhibited superior fatigue strengths compared to bainitic–ferritic steel. Moreover, the introduction of nitrogen led to notable enhancements in the fatigue properties of the UHSS.

Building on this foundation of research, Guo et al. [20] implemented diverse treatment processes aimed at improving the toughness and fatigue life of UHSSs. This study aimed to optimise material characteristics for enhanced structural performance.

In a previous study by Ali et al. [21], two UHSSs with distinct alloying contents of C, Cr, and Ni underwent different processing routes to promote disparate phase structures, namely martensitic and martensitic–bainitic structures. The present study serves as a continuation of this research, with the objective of exploring the fatigue behaviour and crack initiation mechanism of these two UHSSs characterised by varying chemical compositions and microstructural constituents.

This study contributes to the existing literature by providing a detailed comparative analysis of the fatigue resistance, damage mechanisms, and failure modes of two LA-UHSSs: fully martensitic steel and martensitic–bainitic steel. By utilising advanced microscopic techniques such as laser scanning confocal microscopy and scanning electron microscopy, this study tracked the microstructure evolution and fracture surface characteristics during cyclic loading. Additionally, the cyclic hardening and softening behaviours of these steels were evaluated using microindentation hardness tests. The identification of NMIs and their role in fatigue crack initiation, along with the chemical composition analysis of these inclusions, further enhances our understanding of the factors that influence fatigue performance. Ultimately, this research aims to provide valuable insights into the fatigue behaviour of low-alloyed UHSSs, informing future material designs and applications in industries that require high-strength and fatigue-resistant materials.

## 2. Experimental Procedures

### 2.1. Materials

Two low-alloy steels representative of ultrahigh-strength steels (UHSSs) were specifically designed for this experimental study. The manufacturing process began by melting the materials in an air induction furnace. The resulting molten alloys were then subjected to hot forging within a temperature range of 1100–950 °C followed by air cooling, enabling the production of bars with a cross-section of 28 mm × 30 mm. The chemical compositions of the UHSS samples investigated in this study are listed in Table 1.

**Table 1.** Chemical composition of the investigated steels (wt.%).

	C	Si	Mn	P	S	Cr	Mo	Ni	W	V	N
Steel A	0.30	0.71	0.70	0.02	0.02	2.32	0.32	2.34	1.21	0.08	0.01
Steel B	0.15	0.51	0.41	0.02	0.02	1.73	0.31	4.44	1.33	0.07	0.02

### 2.2. Fatigue Tests

Fatigue specimens were prepared according to the guidelines specified in ASTM E466-07 [22]. These specimens took the form of cylindrical tubes with dimensions measuring Ø11 mm in diameter and a total length of 120 mm, ensuring alignment parallel to the rolling direction of the UHSS plates. Within each specimen, a gauge length zone was established, measuring Ø5 mm in diameter and 12 mm in length. For a visual representation of the fatigue sample geometry and dimensions, please refer to Figure 1, where all measurements are in millimetres (mm). Fatigue tests were conducted using a force-controlled method with cyclic tension–compression loading and a constant-amplitude sinusoidal load at a frequency of 100 Hz. The tests were conducted at room temperature under ambient air conditions using an Instron hydraulic fatigue machine equipped with an Instron 8800

controller (Instron, Norwood, MA, USA), which offered a maximum load capacity of 250 kN. A stress ratio of  $-1$  was employed for all fatigue tests. To ensure the accuracy and reliability of the fatigue results, it was necessary to eliminate any potential effects of surface machining on the samples. The surface strain and roughness resulting from the machining processes can introduce additional stress concentrations and alter the fatigue behaviour. Therefore, electropolishing was selected as the method for removing surface imperfections. In this study, the fatigue limit ( $\sigma_{FL}$ ) was determined as the average of the maximum stress amplitudes sustained by three fatigue specimens without failure.

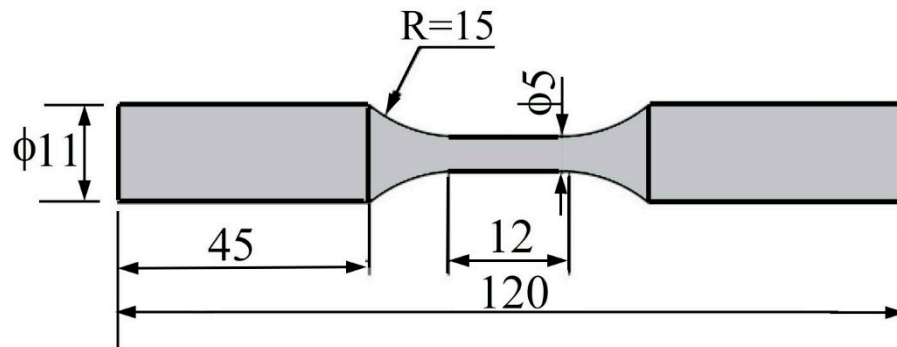


**Figure 1.** Specimen geometry and dimensions for fatigue tests (unit: mm).

### 2.3. Characterisation

The fracture surfaces of the specimens that failed under cyclic straining were examined using field emission gun scanning electron microscopy (FEG-SEM) (Carl Zeiss Ultra Plus, Oberkochen, Germany). Electron backscatter diffraction (EBSD) analysis was conducted at an accelerating voltage of 20 kV to examine the characteristics of the initial microstructures of both steel types after undergoing chemical polishing using a 0.05  $\mu\text{m}$  colloidal suspension of silica for about 10 min. The EBSD maps were processed using HKL software-Channel 5 to identify coexisting phases and provide high-resolution crystallographic information.

The size and shape of the NMIs were investigated using an automated serial sectioning technique with RoboMET.3D™ (UES, Inc. Dayton, Ohio, USA). The automated sectioning procedures included layer-by-layer material removal and polishing up to 1  $\mu\text{m}$ , followed by ultrasonic cleaning in ethanol. The removal height for each layer was automatically recorded using the autofocus feature. Serial sectioning was conducted for 72 layers, and image segmentation was performed to identify individual NMIs. Reconstruction of the segmented regions showing the NMIs was carried out using Dream3D software v6.5 [23], and visualisation was performed using ParaView 5.12.0 software. Energy-dispersive X-ray spectroscopy (EDS) integrated with FEG-SEM was used to determine the chemical composition of the NMIs. SEM was operated at an accelerating voltage of 15 kV to ensure optimal resolution and accurate detection of the elemental constituents present in the inclusions. Microindentation hardness ( $H_{IT}$ ) measurements of the steels before and after cyclic straining were performed to assess their cyclic deformation responses.  $H_{IT}$  tests were conducted using a microindentation hardness tester (CSM Instruments of Anton Paar GmbH, Peseux, Switzerland) equipped with a Berkovich indenter. The tests involved increasing the load to a maximum force of 2 N at loading and unloading rates of 66.66 mN/s, with a holding time of 15 s. This process allowed the acquisition of force–penetration depth (PD) curves up to a maximum indentation force of 2 N during the loading–unloading cycles.

## 3. Results and Discussion

### 3.1. Microstructure Characteristics

The variation in the chemical compositions of the studied steels primarily influenced the adjusted microstructures. Steel A was designed with a high C content of 0.3 wt.% and a lower Ni content of 2.3 wt.%, to promote a predominant matrix of lath martensitic structure. In contrast, Steel B was formulated with a relatively low C content of 0.15 wt.% and a

higher Ni content of 4.44 wt.%, to enhance the formation of a lower bainite phase within a martensitic matrix. Different concentrations of alloying elements also affected the bainite and martensite start temperatures of the respective alloys.

The EBSD inverse pole figure (IPF) maps of Steels A and B, shown in Figure 2a,d, respectively, illustrate the characteristic lath martensitic morphology. Steel B exhibited slightly larger laths and effective grain sizes than Steel A. This difference in lath size and thickness can be attributed to variations in prior austenite grain size (PAGS), which is influenced by the pinning effect of the alloying precipitates.

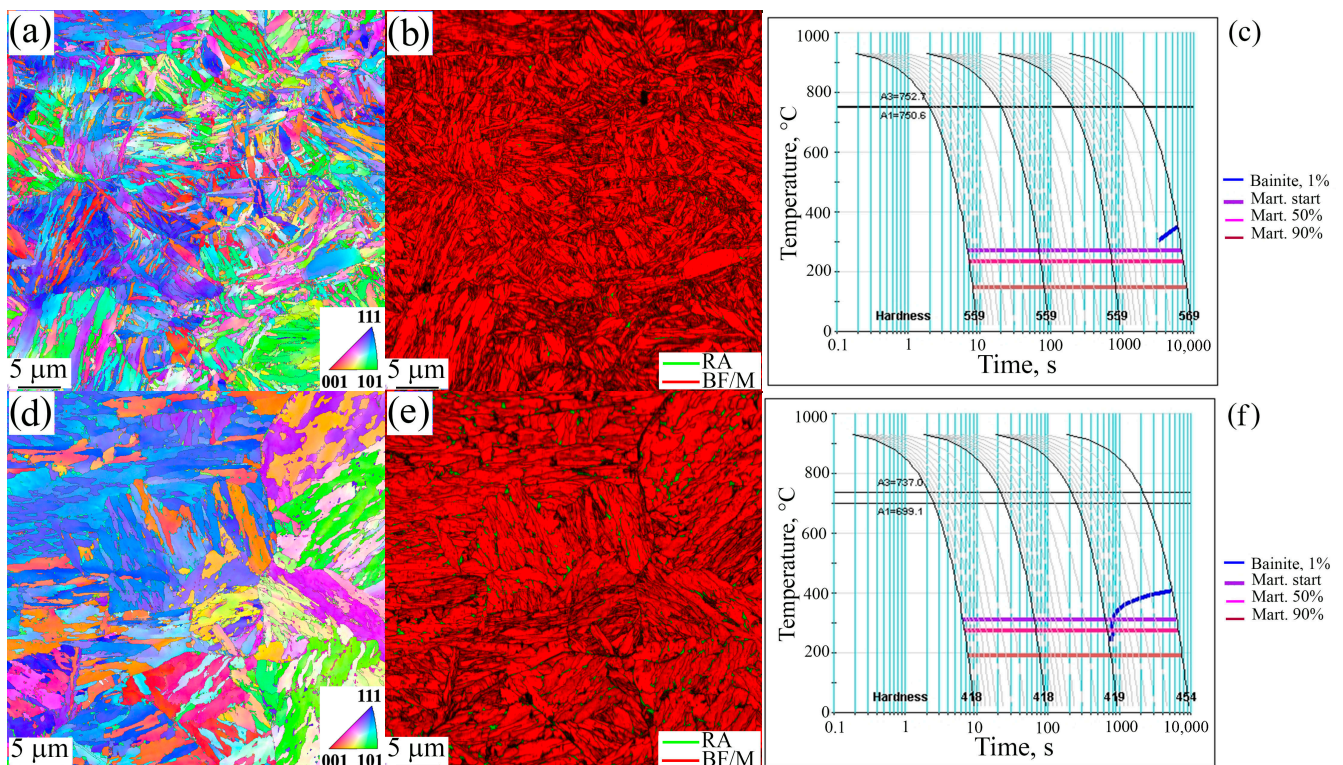


**Figure 2.** Microstructural characterisation of the investigated ultrahigh-strength steels: (a,d) EBSD-IPF maps illustrating the lath structures of Steel A and Steel B, respectively. (b,e) Phase maps highlighting the distribution of phases in Steel A and Steel B, respectively. (c,f) CCT diagrams predicted by JMatPro software v12.2, showcasing the transformation behaviour of Steel A and Steel B, respectively.

Figure 2b shows the phase map of Steel A, indicating the presence of only a martensitic (M) matrix. Conversely, the phase map of Steel B (Figure 2e) demonstrates the existence of approximately 6 vol.% inter-lath retained austenite (marked in green) within the martensitic-bainitic M/B matrix. These distinctions in the phase distribution are primarily attributed to differences in the chemical compositions, aligned with the predictions of the JMatPro software v12.2 (Sente Software Ltd., Oxford, UK), as shown in Figure 2c,f.

To examine the detailed morphological features of the different phases present in Steel A and B, high-resolution SEM imaging using an in-lens detector was employed. Figure 3a showcases the microstructure of Steel A, revealing ridge-like regions composed of fine martensite laths. These laths are aligned in clusters, contributing to the overall strength and hardness of the material. In contrast, Figure 3b presents the microstructure of Steel B, where a broken lath-like morphology is predominant within the lath structure. This observation suggests the presence of a significant fraction of bainite, comprising approximately 52% of the microstructure, along with a tempered martensite matrix. Colour etching was employed to quantify the bainite volume fraction in martensite and bainite microstructures. The specimens underwent etching with a 4% picric acid solution, followed

by a 10% aqueous sodium metabisulfite solution. For a more comprehensive analysis of the microstructure and NMIs characteristics, please refer to our previous publications [21].

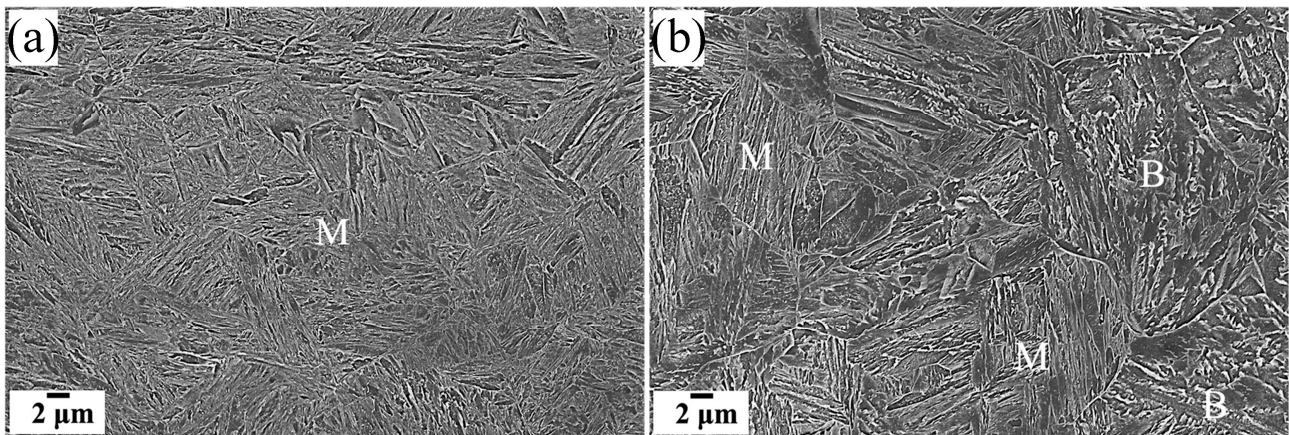


**Figure 3.** High-magnification SEM images of the studied steels using an in-lens detector: (a) Steel A revealing a lath martensitic structure, and (b) Steel B exhibiting a bainite phase and the fragmented lath-like morphology of tempered martensite. (M and B represent martensite and bainite, respectively).

The differences in the phase distributions of Steels A and B can be primarily attributed to the variations in their chemical compositions. Steel A with a carbon content of 0.30 wt. % is specifically designed to enhance hardenability and strength through controlled phase transformations. These transformations involve lowering the temperature at which martensite forms [24,25], resulting in a fine and well-dispersed martensitic structure. In addition, solid-solution strengthening and carbide precipitation further contribute to the mechanical properties of Steel A.

Steel B exhibits a complex microstructure owing to its composition. The presence of bainite, characterised by its distinctive lath-like morphology, introduces a degree of toughness and ductility to the material. The tempered martensite matrix provides additional strength and stability.

The observed differences in the microstructures of Steels A and B highlight the influence of chemical composition on the resulting phases and their morphologies. These variations have significant implications for the mechanical properties and performance of the respective steels. These issues are discussed in detail in Section 3.2.

### 3.2. Tensile Properties and Microindentation Hardness

The tensile properties of the studied steels were examined through uniaxial tension tests, which provided insights into their mechanical behaviour under applied forces, as shown in Figure 4. Steel A, characterised by a martensitic structure, displayed superior yield strength (YS) and ultimate tensile strength (UTS) compared to Steel B, which had a martensitic–bainitic structure.

Steel A exhibits a YS of 1145 MPa, indicating the stress level at which the material begins to deform plastically. This higher YS suggests that Steel A has greater resistance to deformation and can withstand higher loads before undergoing plastic deformation. Similarly, the UTS of Steel A, measured at 1872 MPa, indicates the maximum stress that the material can withstand before fracture. A higher UTS suggests that Steel A possesses enhanced strength and can endure greater tensile loads before failure occurs.

In contrast, Steel B, with its martensitic–bainitic structure, exhibited slightly lower YS and UTS values. Steel B exhibited a YS of 920 MPa, indicating a lower resistance to plastic deformation than Steel A. Similarly, the UTS of Steel B, measured at 1353 MPa, indicated a slightly lower maximum stress capability before fracture than that of Steel A.

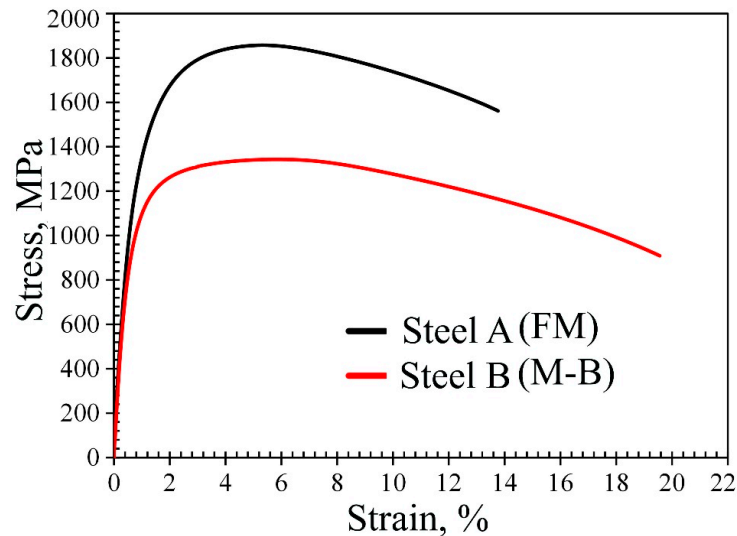


**Figure 4.** Tensile engineering stress–strain curves of the investigated ultrahigh-strength steels (UHSSs): Steel A (fully martensitic steel) and Steel B (martensitic–bainitic steel).

These differences in the tensile properties can be attributed to variations in the microstructure and phase constituents of the two steels. The martensitic structure of Steel A, with its lath-like morphology, provided a higher density of dislocations [26,27], leading to increased strength. In contrast, the martensitic–bainitic structure of Steel B, characterised by a combination of laths and bainitic regions, may result in a slightly lower strength owing to the presence of a relatively softer bainitic phase.

The tensile test results indicated that Steel A exhibited higher yield and tensile strengths than Steel B. Kumar et al. [28] conducted a study that investigated the impact of the bainite/martensite content on the tensile properties of low-carbon high-strength steel. Their findings demonstrated that the martensitic phase exhibited a higher strength but lower ductility than steels with an equivalent volume fraction of bainite.

The  $H_{IT}$  tests were performed to evaluate the hardness properties of Steel A and Steel B. Figure 5 illustrates the loading–unloading curves obtained from these tests, providing valuable insights into the behaviour of the materials during the indentation process.

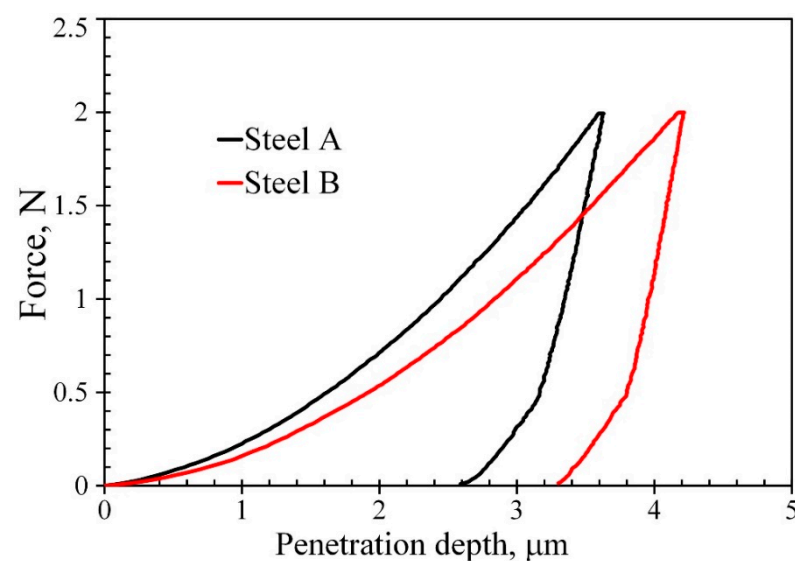


**Figure 5.** Load–penetration depth (P-h), loading–unloading curves of HIT measurements for the studied ultrahigh-strength steels. (Steel A: fully martensitic, Steel B: martensitic–bainitic).

Upon analysis of the results, it was evident that Steel A (black curve) displayed a lower PD of 2.9  $\mu\text{m}$  compared to Steel B (red curve). This indicates that Steel A exhibited higher resistance to deformation during penetration, highlighting its superior hardness characteristics. Conversely, Steel B exhibited a relatively higher PD of 3.6  $\mu\text{m}$ , suggesting a lower resistance to deformation during indentation.

The  $H_{IT}$  values for Steel A and Steel B were determined to be  $7.7 \pm 0.36$  GPa and  $5.24 \pm 0.23$  GPa, respectively. These values are consistent with the tensile properties of both steels, as shown in Figure 3. The observed differences can be attributed to the phase constituents of the studied steels. Steel A predominantly consists of a hard lath martensitic phase, whereas Steel B contains softer phases, such as 6% retained austenite and 52% bainite. As a result, the mechanical strength and  $H_{IT}$  of Steel B were lower than those of Steel A. Similarly, Haiko et al. [29] measured the bulk hardness of high-strength martensitic steel processed using direct quenching and partitioning, as well as for bainitic steel with a similar chemical composition. Their study revealed that the martensitic steel exhibited higher hardness than the bainitic steel.

These findings highlight the correlation among the microindentation hardness values, tensile properties, and phase constituents of steels. Microindentation hardness tests provide valuable insight into the hardness characteristics of a material, which are influenced by the composition and phase distribution within the steel microstructure.

### 3.3. Fatigue Behaviour

The fatigue performance of a material is a critical factor in determining its reliability and durability under cyclic loading. The S–N curve plotted in Figure 6 illustrates the relationship between the stress amplitude and the number of cycles to failure for the investigated steels.

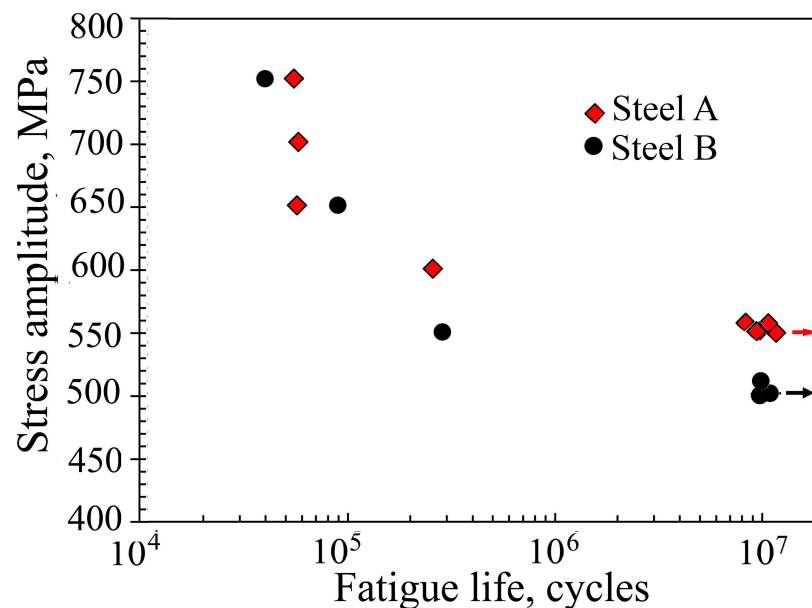


**Figure 6.** Fatigue life data (S–N curves) showing the relationship between stress amplitude and the number of cycles to failure for the tested UHSSs (Steel A: martensitic matrix–red; Steel B: martensitic–bainitic matrix–black).

Steel A, characterised by a martensitic matrix, exhibited higher fatigue resistance than Steel B, which had a martensitic–bainitic structure. This difference can be attributed to variations in their microstructural features and phase constituents [30]. The martensitic structure of Steel A, with its lath-like morphology, provided a higher density of dislocations, resulting in improved fatigue performance. However, Steel B, with its martensitic–bainitic

structure, may have relatively softer bainitic regions, which can contribute to slightly lower fatigue resistance.

The fatigue limits, estimated as the stress levels at which failure did not occur within  $10^7$  cycles, were 550 MPa for Steel A and 500 MPa for Steel B. These values indicate the maximum stress amplitudes that the material can withstand for an extended number of cycles without failure.

Furthermore, the fatigue–strength ratio ( $\sigma_{FL}/\sigma_{TS}$ ), where  $\sigma_{FL}$  is the fatigue limit and  $\sigma_{TS}$  is the tensile strength, is commonly used to assess the fatigue performance of materials. It has been established that this ratio typically falls within the range of 0.4 to 0.6 [31]. However, the estimated ratios for UHSSs A and B were found to be 0.29 and 0.37, respectively, which are noticeably lower than the conventional range. These observations align with the findings of Yu et al. [8], who studied UHSSs with a tensile strength of 2 GPa and reported a  $\sigma_{FL}/\sigma_{TS}$  ratio of approximately 0.34. This suggests that the studied UHSSs may possess significant defects or other factors that contribute to their relatively lower fatigue strengths compared to the reported values for other steels.

These findings highlight the importance of understanding the fatigue behaviour and failure mechanisms of UHSSs to improve their fatigue resistance and overall performance. Further investigations are warranted to identify and address the factors contributing to the observed lower fatigue–strength ratios and to explore potential strategies for enhancing the fatigue performance of UHSSs.

Extensive analysis using secondary electron imaging was performed to gain deeper insights into the mechanism of fatigue damage. The fracture surface of Steel A, tested at a stress level of 600 MPa, is presented in Figure 7. Upon closer examination of the fracture surface (Figure 7a), three distinct zones can be identified: the crack initiation zone (highlighted by a yellow circle), the crack propagation zone (indicated by arrows), and the overloaded zone. To conduct a thorough investigation of the crack initiation site, a high-magnification image was captured and is presented in Figure 7b. The image reveals the presence of an NMI composed of globular oxides with a relatively large size of approximately  $160\ \mu\text{m}$ . Upon closer examination, it is evident that the NMI has experienced breakage and decohesion from the steel matrix, likely due to localised stress concentration. Song and Sun [32] postulated that the localised strain concentration, induced by factors such as non-metallic inclusions or microstructural irregularities, leads to a progressive accumulation of irreversible plastic deformation within the material. This process, in turns, initiates the formation of microcracks at these sites.

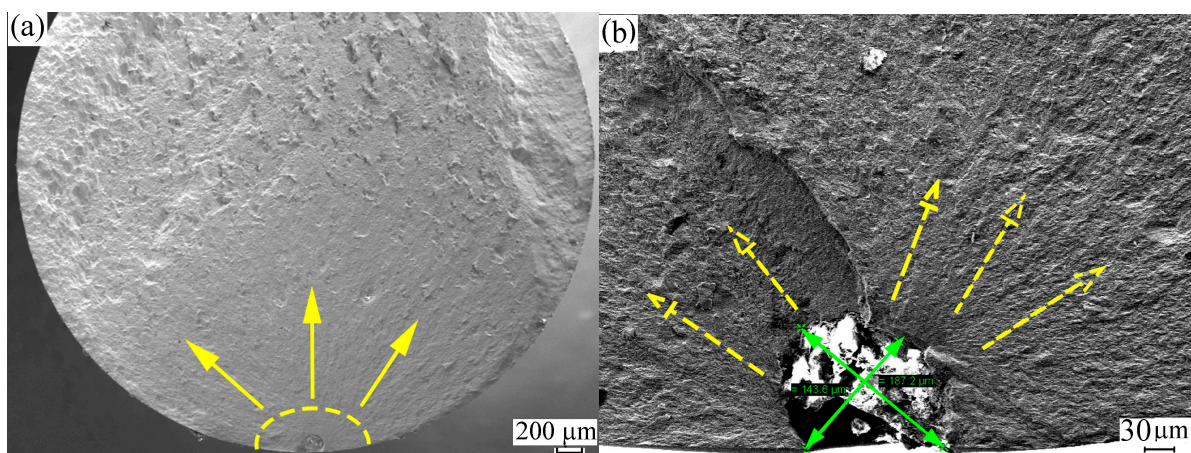


**Figure 7.** Fracture surface analysis of Steel A (martensitic matrix) revealing fatigue damage mechanism at a stress amplitude of 600 MPa: (a) overview of the fracture surface; (b) high-magnification image highlighting the fatigue initiation site (dashed yellow circle in (a)). The arrows show the crack propagation.

The elemental analysis using EDS provided detailed information about the chemical composition of the NMI present at the fatigue crack initiation site. In Figure 8, the EDS element distribution maps show the spatial distribution of different elements at the fatigue crack initiation site. The analysis reveals high concentrations of oxygen (O), silicon (Si), and manganese (Mn) elements in the area surrounding the crack initiation site. This information suggests that the NMI responsible for the fatigue damage contains a significant amount of complex Mn/Si oxides.

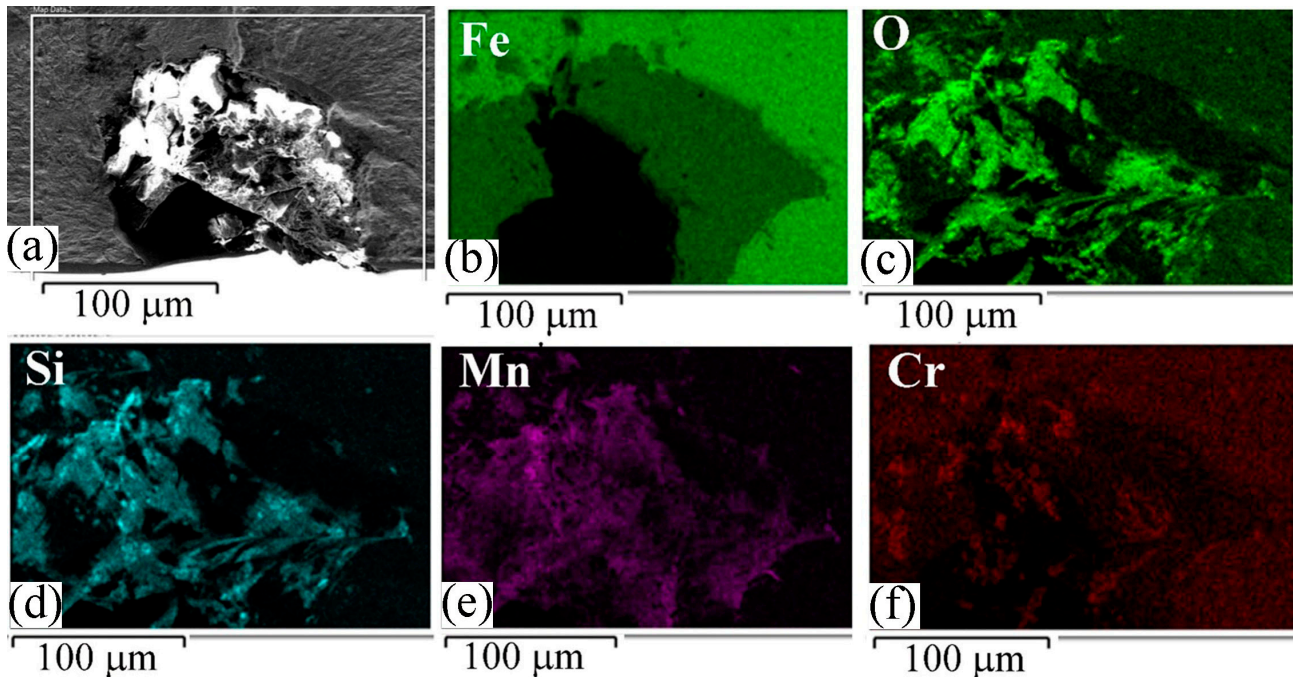


**Figure 8.** EDS elemental distribution maps of the NMI responsible for fatigue crack initiation in Steel B at stress amplitude 600 MPa: (a) SEM image of the analysed region, (b) Fe distribution map, (c) O distribution map, (d) Si distribution map, (e) Mn distribution map, and (f) Cr distribution map.

The presence of these specific elements in NMI is crucial for understanding the fatigue behaviour of the material. NMIs with these compositions can act as stress concentrators and promote crack initiation during cyclic loading.

Moreover, various internal inclusion defects (highlighted by circles in Figure 9) were identified within the fracture surface. In Figure 9a, the presence of a void surrounding a MnS inclusion is evident, as confirmed by the EDS analysis displayed in the upper right corner of the image. This observation suggests that the internal inclusion may contribute to the development of fish-eye-type cracking, a characteristic feature of fatigue failure [15]. In another instance shown in Figure 9b, an internal inclusion consisting of MnO and SiO<sub>2</sub>, is observed in a different sample tested at a stress level of 650 MPa. Interestingly, a fatigue crack is observed to originate from this large NMI located within the interior matrix. This finding further emphasises the significance of NMIs as the primary source of fatigue failure in Steel A. The presence of these internal inclusions provides critical sites for crack initiation, leading to the initiation and propagation of fatigue cracks during cyclic loading, ultimately impacting the material's fatigue behaviour.

During cyclic loading, cracks are initiated and propagated from broken internal defects or are caused by the detachment of inclusions from the steel matrix. The initiation of subsurface cracks and the growth of internal microstructural short cracks significantly contribute to the fatigue life of the material. These findings were consistent with those reported by Burkart et al. [33]. In the same context, Zhang et al. [34] revealed that high-purity UHSSs containing inclusions smaller than 1 µm demonstrate substantially higher

fatigue strengths when compared to those with larger inclusion sizes of approximately 30  $\mu\text{m}$ .

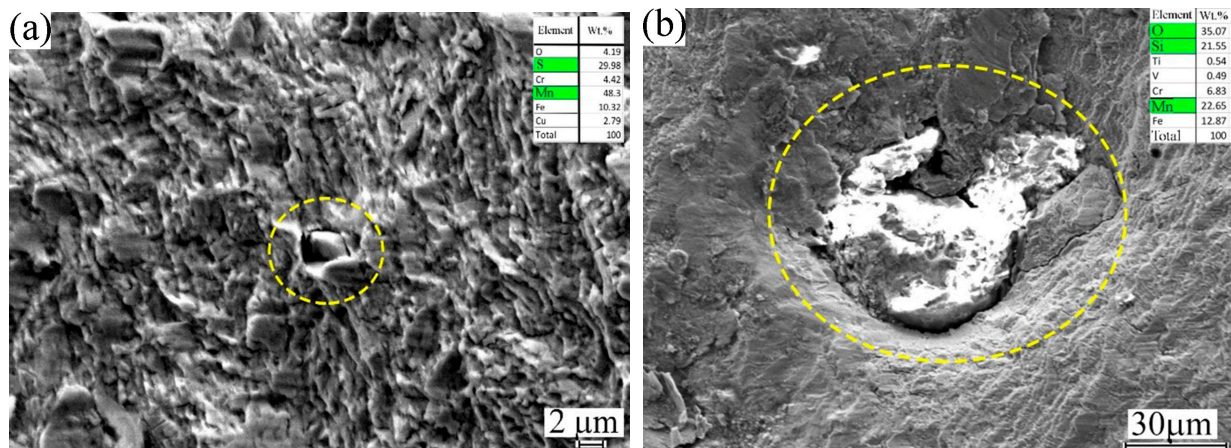


**Figure 9.** Fracture surface analysis of Steel A (martensitic matrix) revealing a fatigue damage mechanism at internal defects: (a) observation of internal MnS NMI, highlighted by a dashed circle, at a stress amplitude of 600 MPa and (b) fatigue initiation site at internal Mn/Si oxide NMI, highlighted by a dashed circle, at a stress amplitude of 650 MPa.

The fracture surface analysis of Steel B with a martensitic–bainitic multiphase structure provides further insights into the fatigue damage mechanism. In Figure 10a, it is observed that an NMI at the surface serves as the initiation site for the fatigue crack, and the fatigue crack propagates through the matrix, as indicated by the arrows. This inclusion acts as a stress concentrator, leading to localised cyclic plastic deformation during fatigue loading [35]. The cyclic plastic deformation accumulates at these inclusion sites, eventually resulting in crack initiation. In this study, conducted by Mayer et al. [36] on high-cycle fatigue properties of bainitic steel, they observed that 42% of the fractured specimens exhibited crack initiation at internal  $\text{Al}_2\text{O}_3$  inclusions, while in 58% of cases, cracks were initiated at the surface, particularly at scratches or cavities resulting from grinding. Notably, the presence of internal inclusions was found to induce fracture initiation, leading to shorter lifetimes for the specimens.

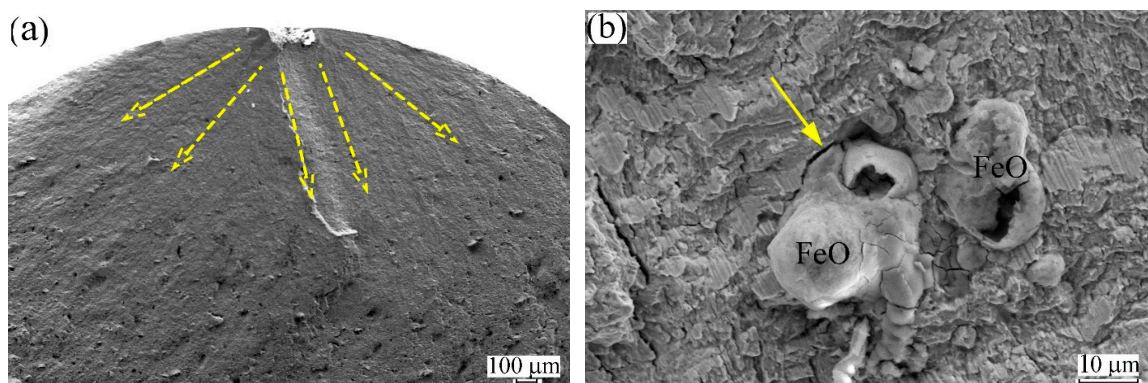


**Figure 10.** SEM images of the fracture surfaces of steel B at a stress amplitude of 650 MPa: (a) fatigue crack initiation site and propagation, highlighted by the dashed arrows, correlated with a NMI at the surface and (b) interior FeO inclusion displaying decohesion of the matrix, highlighted by the yellow arrow.

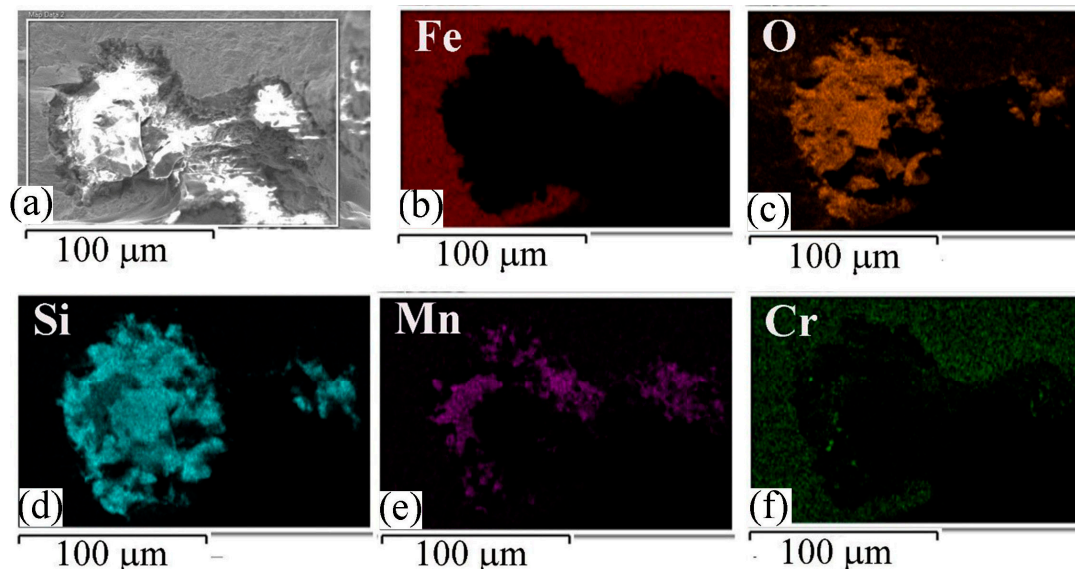
Figure 10b shows the presence of interior FeO inclusions in the crack propagation zone. Additionally, fine striations and traces of slip lines were observed in this region, as

indicated by the arrows. These features indicate the cyclic slip irreversibility of dislocations and highlight the cyclic deformation behaviour and ductility of the steel matrix.

Steels A and B exhibited similar fatigue mechanisms, where NMIs played a crucial role in crack initiation. However, Zhao et al. [37] reported an additional mechanism for Steel B. During the cyclic straining, the dual-phase matrix experienced significant plastic deformation within the bainite components. This leads to the promotion of “debonding” from the adjacent martensite and the initiation of microcracks at the boundaries between bainite laths and martensite.

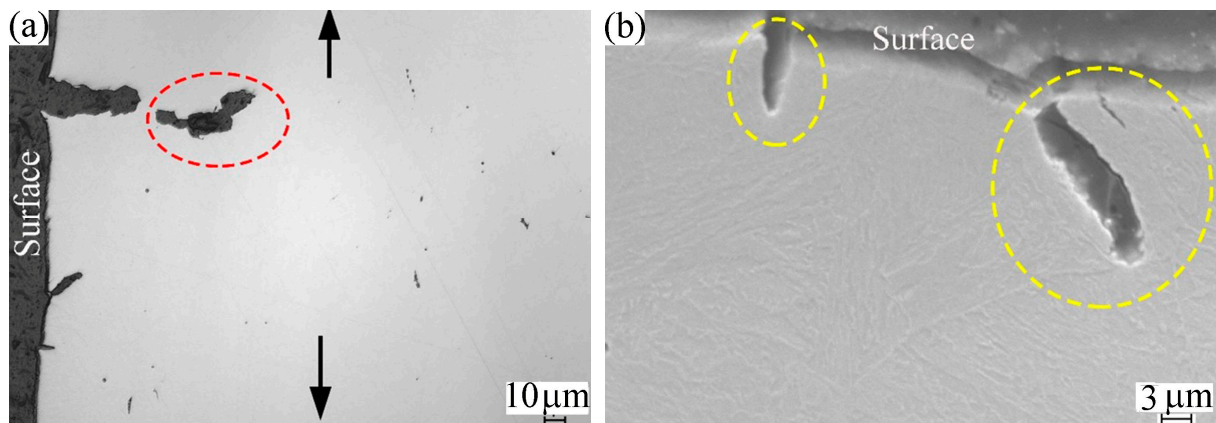
It is apparent that the fatigue damage mechanism in both Steels A and B involves the initiation of cracks at the NMIs, whereas Steel B exhibits additional complexities owing to the existence of a dual-phase structure, comprising bainite and martensite, with different mechanical behaviours.

Figure 11 illustrates the elemental maps of the NMI responsible for the fatigue crack initiation site shown in Figure 10. The analysis reveals that the NMI primarily consists of O, Si, and Mn, indicating the presence of Mn/Si oxides.



**Figure 11.** EDS elemental distribution maps of the NMI responsible for fatigue cracking initiation in Steel B at stress amplitude 650 MPa: (a) SEM image of the analysed region, (b) Fe distribution map, (c) O distribution map, (d) Si distribution map, (e) Mn distribution map, and (f) Cr distribution map.

Remarkably, surface cracks are evident in the cross-section of the fatigued Steel B, as illustrated in Figure 12a. Previous research by Mayer et al. [38] has indicated that surface cavities and scratches resulting from grinding can be favoured sites for crack initiation on the surface. However, to mitigate this effect, we applied electropolishing in this study. Interestingly, such surface cracks were not observed in the harder Steel A. An internal crack, highlighted within a red circle, is clearly visible in Steel B. It is reasonable to attribute this internal crack to the presence of the NMI. Upon closer examination by SEM at a high magnification, Figure 12b displays surface cracks oriented at a 45° angle to the loading direction. Furthermore, fine microcracks are observed in parallel to the larger surface crack, as highlighted by the yellow circle. Given the ductility and phase structure of Steel B, well-defined distributed fatigue markings, such as the characteristic features of persistent slip bands (PSBs) in fatigued polycrystalline bcc metals, can be identified [39,40]. These PSBs represent localised strained regions that can induce additional fatigue cracks.



**Figure 12.** Microstructural analysis of fatigued Steel B (martensitic–bainitic matrix) cross-section: (a) surface cracks and internal crack attributed to the NMI; (b) high-magnification SEM image showing surface cracks oriented at  $45^\circ$  to the loading direction and distributed fatigue markings indicative of persistent slip bands (PSBs).

The three-dimensional morphology and size of NMIs in the studied steel were determined by constructing the obtained microscopy images taken using a serial sectioning RoboMET.3D microscope. This advanced tool enabled a detailed analysis of the size, shape, and distribution of NMIs within the steel matrix, providing crucial insights into their role in fatigue failure. Figure 13a shows a general view in 2D of the microstructure of Steel A at a low magnification. Two large black spots, highlighted as I and II by yellow circles, are observed. The 3D views of I and II displayed large NMIs with irregular shapes with a height of  $300\ \mu\text{m}$ , as illustrated in Figure 13a,b. This NMI morphology and the large interface boundaries within the steel matrix are critical as they influence the local stress concentrations, which in turn affect crack initiation and propagation during cyclic loading. This detailed morphological analysis supports the conclusion that NMIs are pivotal in determining the fatigue resistance of UHSSs, particularly in how they act as stress concentrators that facilitate localised plastic deformation and crack initiation in the HSSs.

The  $H_{IT}$  tests were conducted on the studied steels following fatigue testing. These tests were performed on the gauge section of the specimen, specifically in the central region where fatigue deformation is influenced and uniform. The loading–unloading curves were analysed and compared, as depicted in Figure 14. Surprisingly, the P–h (force–penetration depth vs. load) curves for both steels appeared to be quite similar, indicating that there was only a negligible difference in the  $H_{IT}$  values after fatigue.

However, closer examination revealed distinct changes in the  $H_{IT}$  values of the individual steels after fatigue. Steel A, known for its inherent hardness, exhibited a significant decrease in the  $H_{IT}$  value, dropping from  $7.7 \pm 0.36\ \text{GPa}$  (as observed before fatigue, Figure 5) to  $5.66 \pm 0.26\ \text{GPa}$  after fatigue testing. This substantial reduction in the hardness of Steel A suggests that it experienced cyclic softening during cyclic straining.

In contrast, Steel B exhibited contrasting behaviour. It showed a slight cyclic hardening effect, with its  $H_{IT}$  value increasing from  $5.24 \pm 0.23\ \text{GPa}$  before fatigue to  $5.41 \pm 0.31\ \text{GPa}$  after fatigue. This minor increase in hardness indicates that Steel B became slightly harder during fatigue testing.

To quantify these cyclic hardening/softening effects, we calculated the cyclic hardening/softening ratio based on the difference in the hardness before and after fatigue testing. We should emphasise that this study employed force-controlled fatigue tests, which do not allow for the generation of cyclic hardening/softening curves. The cyclic behaviour results are, therefore, based on the hardness measurements after fatigue rather than strain-controlled tests.

For Steel A, the cyclic softening ratio is approximately 27%, indicating a substantial decrease in hardness. In contrast, Steel B exhibited a relatively small cyclic hardening ratio of 4%, indicating a modest increase in hardness after fatigue.

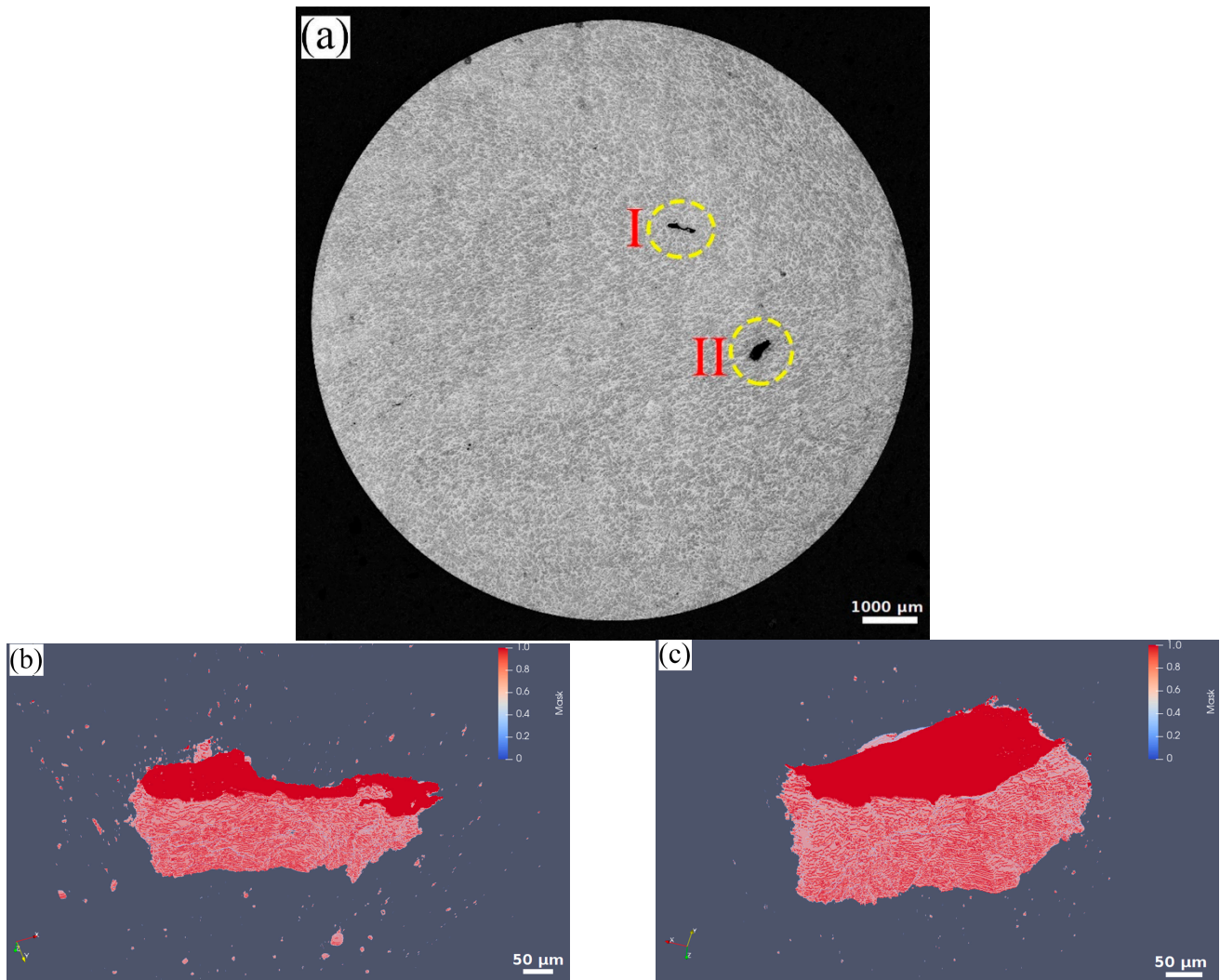


**Figure 13.** Three-dimensional morphology of non-metallic inclusions (NMIs) in Steel A, captured by the Robo-Met.3D microscope. (a) General 2D view, (b) magnified view of NMI marked as I in (a) and (c) magnified view of NMI marked as II in (a).

These findings provide significant insights into fatigue-induced changes in the hardness of the studied steels. Steel A exhibited a notable decrease in hardness owing to cyclic softening, whereas Steel B experienced a minor increase in hardness with slight cyclic hardening. These differences in the material response to cyclic loading underscore the importance of considering the unique mechanical behaviour and material properties of each steel when evaluating its fatigue performance.

Cyclic strain hardening is typically observed in initially soft materials, while cyclic strain softening is more common in materials that are already hardened [41]. In the case of hard Steel A, during cyclic deformation, the stress and strain concentrations around dislocations can trigger structural changes in the material. These changes, such as dislocation rearrangements and annihilation of these dislocations through recovery processes, help dissipate the accumulated energy within the material, resulting in the relaxation of potential energy in the matrix [42].

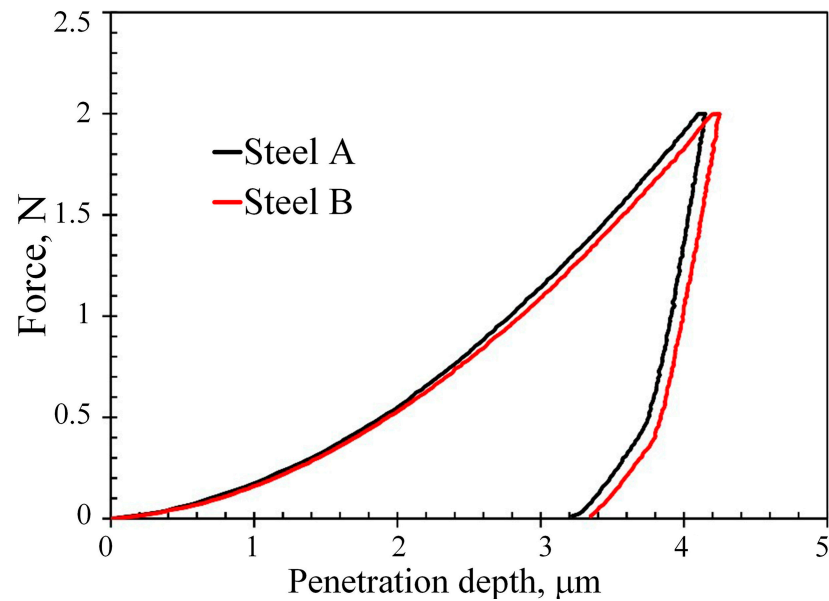


**Figure 14.** Load–penetration depth (P-h) curves from microindentation hardness tests conducted on martensitic Steel A (black curve) and martensitic–bainitic Steel B (red curve) after cyclic plastic deformation.

Hence, the structural changes and energy relaxation processes lead to a reduction in the density and activity of dislocations within the material. As the dislocations were annihilated or rearranged during cyclic loading, the dislocation density of the material decreased, resulting in a softer matrix. This led to the observed cyclic softening effect in hard Steel A.

#### 4. Conclusions

This study provides valuable insights into the microstructural characteristics, tensile properties, and fatigue behaviour of martensitic and martensitic–bainitic UHSSs. The role of NMIs in fatigue failure is emphasised, and the complexities of fatigue behaviour in martensitic–bainitic UHSSs are highlighted. The following conclusions were drawn from our findings:

1. Steel A, with its martensitic structure, exhibited higher YS and tensile strength (UTS) compared to Steel B, which has a martensitic–bainitic structure. The YS and UTS values for Steel A were measured to be 1145 and 1872 MPa, respectively, while the corresponding values for Steel B were 920 and 1353 MPa.
2. Fatigue tests revealed that Steel A demonstrated higher fatigue resistance compared to Steel B. The fatigue limit ( $\sigma_{FL}$ ) for Steel A and Steel B was estimated to be 550 and 500 MPa, respectively, corresponding to a fatigue run out of  $10^7$  cycles without failure.
3. NMIs acted as stress concentrators, leading to localised cyclic plastic deformation and fatigue crack initiation. Chemical analysis revealed Mn/Si oxides as the primary constituents of the NMIs.
4. Surface cracks were observed in the cross-section of fatigued Steel B, while internal cracks were attributed to NMIs. Microstructure investigations showed surface cracks and distributed fatigue markings (PSBs) in Steel B, highlighting its complex fatigue behaviour.

**Author Contributions:** Conceptualisation, A.H., M.A. and S.G.; methodology, A.H., M.A., S.G., M.E., T.M. and R.S.; Software, M.J., T.A. and S.G.; validation, A.H. and M.J.; formal analysis, A.H. and T.A.; investigation, A.H., M.A. and M.J.; resources, R.S., M.E. and T.M.; data curation, A.H., M.A., M.J. and T.A.; writing—original draft preparation, A.H.; writing—review and editing, A.H., M.A., R.S. and T.A.; visualisation, A.H., M.A. and S.G.; supervision, A.H.; project administration, A.H.;

funding acquisition, R.S., M.E. and T.M. All authors have read and agreed to the published version of the manuscript.

**Funding:** This research received no external funding.

**Data Availability Statement:** No new data were created or analyzed in this study. All relevant data are included within this manuscript.

**Acknowledgments:** The authors would like to express their gratitude to the steel lab at CMRDI, Helwan, Egypt, for melting and forging the cast steels. We also extend our thanks to the FMT group at Kerttu Saalasti Institute for funding the fatigue tests and scanning electron microscopy (SEM). Additionally, we would like to acknowledge the Institute of Energy Materials and Devices: Microstructure and Properties of Materials (IMD-1) at Forschungszentrum Jülich GmbH for conducting the RoboMat 3D analysis.

**Conflicts of Interest:** The authors declare no conflicts of interest.

## References

- Dilmore, M.; Ruhlman, J.D. Eglin Steel—A Low Alloy High Strength Composition. US Patent US7537727B2, 26 May 2009. Google Patents. 2009. Available online: <https://patents.google.com/patent/US7537727B2/en> (accessed on 24 July 2023).
- Malakondaiah, G.; Srinivas, M.; Rao, P.R. Ultrahigh-strength low-alloy steels with enhanced fracture toughness. *Prog. Mater. Sci.* **1997**, *42*, 209–242. [[CrossRef](#)]
- Tümer, M.; Schneider-Bröskamp, C.; Enzinger, N. Enzinger, Fusion welding of ultra-high strength structural steels—A review. *J. Manuf. Process.* **2022**, *82*, 203–229. [[CrossRef](#)]
- Hu, L.; Li, X.; Luo, W.; Li, S.; Deng, D. Residual stress and deformation in UHS quenched steel butt-welded joint. *Int. J. Mech. Sci.* **2023**, *245*, 108099. [[CrossRef](#)]
- Tian, J.; Jiang, Z. Exploring New Strategies for Ultrahigh Strength Steel via Tailoring the Precipitates. *Front. Mater.* **2021**, *8*, 797798. [[CrossRef](#)]
- Bhaumik, S.; Sujata, M.; Venkataswamy, M. Fatigue failure of aircraft components. *Eng. Fail. Anal.* **2008**, *15*, 675–694. [[CrossRef](#)]
- Zerbst, U.; Mada, M.; Klinger, C.; Bettge, D.; Murakami, Y. Defects as a root cause of fatigue failure of metallic components. II: Non-metallic inclusions. *Eng. Fail. Anal.* **2019**, *98*, 228–239. [[CrossRef](#)]
- Yu, W.; Zhu, S.; He, X.; Wang, M. Very high cycle fatigue properties of 2000 MPa ultrahigh-strength steels. *Mater. Sci. Technol.* **2022**, *38*, 866–875. [[CrossRef](#)]
- Okuda, K.; Ogawa, K.; Ichikawa, Y.; Shiozaki, T.; Yamaguchi, N. Influence of microstructure on fatigue property of ultra high-strength steels. *Frat. Integrita Strutt.* **2019**, *13*, 125–134. [[CrossRef](#)]
- Schönbauer, B.M.; Ghosh, S.; Karr, U.; Pallaspuro, S.; Kömi, J.; Frondelius, T.; Mayer, H. Mean-stress sensitivity of an ultrahigh-strength steel under uniaxial and torsional high and very high cycle fatigue loading. *Fatigue Fract. Eng. Mater. Struct.* **2022**, *45*, 3361–3377. [[CrossRef](#)]
- Shiozawa, K.; Morii, Y.; Nishino, S.; Lu, L. Subsurface crack initiation and propagation mechanism in high-strength steel in a very high cycle fatigue regime. *Int. J. Fatigue* **2006**, *28*, 1521–1532. [[CrossRef](#)]
- Hong, Y.; Lei, Z.; Sun, C.; Zhao, A. Propensities of crack interior initiation and early growth for very-high-cycle fatigue of high strength steels. *Int. J. Fatigue* **2014**, *58*, 144–151. [[CrossRef](#)]
- Hong, Y.; Liu, X.; Lei, Z.; Sun, C. The formation mechanism of characteristic region at crack initiation for very-high-cycle fatigue of high-strength steels. *Int. J. Fatigue* **2016**, *89*, 108–118. [[CrossRef](#)]
- Furuya, Y.; Matsuoka, S.; Abe, T.; Yamaguchi, K. Gigacycle fatigue properties for high-strength low-alloy steel at 100 Hz, 600 Hz, and 20 kHz. *Scr. Mater.* **2002**, *46*, 157–162. [[CrossRef](#)]
- Jeddi, D.; Palin-Luc, T. A review about the effects of structural and operational factors on the gigacycle fatigue of steels. *Fatigue Fract. Eng. Mater. Struct.* **2018**, *41*, 969–990. [[CrossRef](#)]
- Gui, X.; Gao, G.; An, B.; Misra, R.; Bai, B. Relationship between non-inclusion induced crack initiation and microstructure on fatigue behavior of bainite/martensite steel in high cycle fatigue/very high cycle (HCF/VHCF) regime. *Mater. Sci. Eng. A* **2021**, *803*, 140692. [[CrossRef](#)]
- Liu, C.; Zhao, M.-C.; Zhao, Y.-C.; Zhang, L.; Yin, D.-F.; Tian, Y.; Shan, Y.-Y.; Yang, K.; Atrens, A. Ultra-high cycle fatigue behavior of a novel 1.9 GPa grade super-high-strength maraging stainless steel. *Mater. Sci. Eng. A* **2019**, *755*, 50–56. [[CrossRef](#)]
- Yuan, C.; Li, S.; Huang, J.; Lin, X.; Bian, X.; Chen, J. Effect of hierarchical martensitic microstructure on fatigue crack growth behavior of ultra-high strength hot stamping steel. *Mater. Charact.* **2021**, *174*, 111041. [[CrossRef](#)]
- Hojo, T.; Kobayashi, J.; Sugimoto, K.-I.; Takemoto, Y.; Nagasaka, A.; Koyama, M.; Akiyama, E. Effects of matrix structure and nitrogen content on fatigue properties of ultrahigh-strength low alloy TRIP-aided steels. *Tetsu-to-Hagane/J. Iron Steel Inst. Jpn.* **2021**, *107*, 672–680. [[CrossRef](#)]
- Guo, P.; Deng, L.; Wang, X.; Jin, J. Simultaneous improvement of toughness and fatigue life in a typical ultrahigh strength steel by a new deep cryogenic treatment process. *ISIJ Int.* **2021**, *61*, 463–472. [[CrossRef](#)]

21. Ali, M.; Porter, D.; Kömi, J.; Eissa, M.; El Faramawy, H.; Mattar, T. The Effect of Electroslag Remelting on the Microstructure and Mechanical Properties of CrNiMoWMnV Ultrahigh-Strength Steels. *Metals* **2020**, *10*, 262. [CrossRef]
22. *Designation: E466—07*; Standard Practice for Conducting Force Controlled Constant Amplitude Axial Fatigue Tests of Metallic Materials. ASTM International: West Conshohocken, PA, USA, 2015. [CrossRef]
23. Groeber, M.A.; Jackson, M.A. DREAM.3D: A Digital Representation Environment for the Analysis of Microstructure in 3D. *Integr. Mater. Manuf. Innov.* **2014**, *3*, 56–72. [CrossRef]
24. Totten, G.E. *Steel Heat Treatment: Metallurgy and Technologies*, 1st ed.; CRC Press: Boca Raton, FL, USA, 2006. [CrossRef]
25. Lynch, P.C. *The Development of Ultrahigh Strength Low Alloy Cast Steels with Increased Toughness*; The Pennsylvania State University: University Park, PA, USA, 2011. Available online: <https://ui.adsabs.harvard.edu/abs/2011PhDT.....247L/abstract> (accessed on 25 July 2023).
26. Hamada, A.; Ghosh, S.; Ali, M.; Jaskari, M.; Järvenpää, A. Studying the strengthening mechanisms and mechanical properties of dissimilar laser-welded butt joints of medium-Mn stainless steel and automotive high-strength carbon steel. *Mater. Sci. Eng. A* **2022**, *856*, 143936. [CrossRef]
27. Saha, D.C.; Biro, E.; Gerlich, A.P.; Zhou, Y. Effects of tempering mode on the structural changes of martensite. *Mater. Sci. Eng. A* **2016**, *673*, 467–475. [CrossRef]
28. Kumar, A.; Singh, S.B.; Ray, K.K. Influence of bainite/martensite-content on the tensile properties of low carbon dual-phase steels. *Mater. Sci. Eng. A* **2008**, *474*, 270–282. [CrossRef]
29. Haiko, O.; Pallaspuuro, S.; Javaheri, V.; Kaikkonen, P.; Ghosh, S.; Valtonen, K.; Kaijalainen, A.; Kömi, J. High-stress abrasive wear performance of medium-carbon direct-quenched and partitioned, carbide-free bainitic, and martensitic steels. *Wear* **2023**, 526–527, 204925. [CrossRef]
30. Zhang, Y.; Long, X.; Zhang, Z.; Zhu, R.; Li, Y.; Zhang, F.; Yang, Z. Effect of phase transformation sequence on the low cycle fatigue properties of bainitic/martensitic multiphase steels. *Int. J. Fatigue* **2024**, *178*, 107995. [CrossRef]
31. Chapetti, M.; Miyata, H.; Tagawa, T.; Miyata, T.; Fujioka, M. Fatigue strength of ultra-fine grained steels. *Mater. Sci. Eng. A* **2004**, *381*, 331–336. [CrossRef]
32. Song, Q.; Sun, C. Mechanism of crack initiation and early growth of high strength steels in very high cycle fatigue regime. *Mater. Sci. Eng. A* **2020**, *771*, 138648. [CrossRef]
33. KBurkart, K.; Bomas, H.; Zoch, H.-W. Fatigue of notched case-hardened specimens of steel SAE 5120 in the VHCF regime and application of the weakest-link concept. *Int. J. Fatigue* **2011**, *33*, 59–68. [CrossRef]
34. Zhang, J.M.; Li, S.X.; Yang, Z.G.; Li, G.Y.; Hui, W.J.; Weng, Y.Q. Influence of inclusion size on fatigue behavior of high strength steels in the gigacycle fatigue regime. *Int. J. Fatigue* **2007**, *29*, 765–771. [CrossRef]
35. Nie, Y.H.; Fu, W.T.; Hui, W.J.; Dong, H.; Weng, Y.Q. Very high cycle fatigue behaviour of 2000-MPa ultra-high-strength spring steel with bainite-martensite duplex microstructure. *Fatigue Fract. Eng. Mater. Struct.* **2009**, *32*, 189–196. [CrossRef]
36. Mayer, H.; Haydn, W.; Schuller, R.; Issler, S.; Bacher-Höchst, M. Very high cycle fatigue properties of bainitic high carbon-chromium steel under variable amplitude conditions. *Int. J. Fatigue* **2009**, *31*, 1300–1308. [CrossRef]
37. Zhao, P.; Gao, G.; Misra, R.; Bai, B. Effect of microstructure on the very high cycle fatigue behavior of a bainite/martensite multiphase steel. *Mater. Sci. Eng. A* **2015**, *630*, 1–7. [CrossRef]
38. Mayer, H.; Haydn, W.; Schuller, R.; Issler, S.; Furtner, B.; Bacher-Höchst, M. Very high cycle fatigue properties of bainitic high carbon-chromium steel. *Int. J. Fatigue* **2009**, *31*, 242–249. [CrossRef]
39. Sangid, M.D. The physics of fatigue crack initiation. *Int. J. Fatigue* **2013**, *57*, 58–72. [CrossRef]
40. Armstrong, W.; Polák, J. Role of Persistent Slip Bands and Persistent Slip Markings in Fatigue Crack Initiation in Polycrystals. *Crystals* **2023**, *13*, 220. [CrossRef]
41. Schijve, J. *Fatigue of Structures and Materials*, 2nd ed.; Springer: Delft, The Netherlands, 2009. [CrossRef]
42. Hamada, A.S.; Järvenpää, A.; Ahmed, M.M.Z.; Jaskari, M.; Wynne, B.P.; Porter, D.A.; Karjalainen, L.P. The microstructural evolution of friction stir welded AA6082-T6 aluminum alloy during cyclic deformation. *Mater. Sci. Eng. A* **2015**, *642*, 366–376. [CrossRef]

**Disclaimer/Publisher’s Note:** The statements, opinions and data contained in all publications are solely those of the individual author(s) and contributor(s) and not of MDPI and/or the editor(s). MDPI and/or the editor(s) disclaim responsibility for any injury to people or property resulting from any ideas, methods, instructions or products referred to in the content.